


 Cite this: *RSC Adv.*, 2023, **13**, 24333

# The development of ZnO nanoparticle-embedded graphitic-carbon nitride towards triple-negative breast cancer therapy†

 Varun Prasath Padmanabhan,<sup>‡\*a</sup> Pugalmani Sivashanmugam,<sup>‡b</sup> Mubashera S. M.,<sup>c</sup> Suresh Sagadevan<sup>‡d</sup> and Ravichandran Kulandaivelu<sup>‡\*a</sup>

The present study deals with the effects of curcumin-loaded ZnO nanoparticles (NPs) embedded in graphitic-carbon nitride (g-C<sub>3</sub>N<sub>4</sub>) sheets for breast cancer cells. The synthesis of these sheets was carried out by a simple co-precipitation method. The physicochemical and thermal properties of the composite sheets were studied using various characterization techniques. The powder X-ray diffraction and high-resolution transmission electron microscopy analyses confirmed the hexagonal wurtzite phase of the ZnO nanoparticles, which were randomly distributed on the g-C<sub>3</sub>N<sub>4</sub> nanosheets, generating a finely bonded interface between the two components. The X-ray photoelectron spectroscopy analysis confirmed the successful formation of the g-C<sub>3</sub>N<sub>4</sub>@ZnO composite, while the thermal studies revealed the thermal stability of the composite. In addition, the drug release and kinetics studies proved that the release of curcumin was more significant under acidic conditions (pH 5) compared with neutral pH (7.4). Further, the biological assays verified the antibacterial activity (against two different cultures of *E. coli* and *S. aureus*) and anticancer activity (against MDA-MB-231 cancer cells) of the g-C<sub>3</sub>N<sub>4</sub>@ZnO/C nanocomposite. Finally, the lactate dehydrogenase activity assay presented the cytotoxic assessment of the nanocomposite based on its cytoplasmic activity and the extent of enzymes released from the damaged cells.

 Received 1st May 2023  
 Accepted 28th July 2023

DOI: 10.1039/d3ra02887a

[rsc.li/rsc-advances](http://rsc.li/rsc-advances)

## 1. Introduction

Recent developments in synthesis procedures and characterization techniques have unmasked the active role of many different nanomaterials over a range of biomedical applications, including drug delivery, bioimaging, sensor-based diagnosis, and externally controlled therapy.<sup>1–5</sup> Among the nanomaterials currently applied in the biomedical sector, two-dimensional (2D) layered NPs have gained the most interest because of their unique physicochemical properties linked to their high and efficient surface area along with biocompatibility.<sup>6–8</sup> Typical examples of this type of nanomaterial are graphene and its oxide derivative (graphene oxide; GO), which have already been explored in multiple biological

applications, such as DNA detection,<sup>9,10</sup> cell imaging,<sup>11</sup> drug delivery,<sup>12</sup> photodynamic<sup>13,14</sup> and photothermal therapy.<sup>15</sup> Considering such a strong background of graphene and its derivatives, researchers have developed graphitic carbon nitride (g-C<sub>3</sub>N<sub>4</sub>) with extraordinary features like semiconductivity, favourable electronic structure, chemical and thermal stability, visible light activity, and cost-effectiveness.<sup>16,17</sup> g-C<sub>3</sub>N<sub>4</sub> serves as an active photocatalyst on account of its ~2.7 eV bandgap, enabling the effective excitation of electrons under visible-light irradiation.<sup>18</sup> The quantum efficiency of g-C<sub>3</sub>N<sub>4</sub> is similar to various other photocatalysts in the single-component category and can get degraded easily by the rapid recombination of photo-generated electrons and holes.<sup>19</sup> This can result in the development of photochemically active and stable g-C<sub>3</sub>N<sub>4</sub>-mediated catalysts and hence deserves thorough investigation.

In order to enhance the efficiency of g-C<sub>3</sub>N<sub>4</sub> and overcome its few limitations, researchers have developed heterogeneous composites by the coupling of NPs with g-C<sub>3</sub>N<sub>4</sub>. Nanoparticles are known to be effective in cancer diagnosis and treatment, as they have high surface-to-volume ratios, and the surface is enriched with sites of high coordination and unsaturation.<sup>20</sup> It has been reported that certain metal oxide nanoparticles can destroy cancer cells selectively without harming normal cells.<sup>21</sup> Specifically, ZnO nanoparticles are reported to have high potential in treating cancer due to their intrinsic hydrophilic

<sup>a</sup>Department of Analytical Chemistry, University of Madras, Guindy Campus, Chennai 600 025, India. E-mail: raavees@gmail.com; analvarun@gmail.com

<sup>b</sup>Department of Orthodontics, Saveetha Dental College and Hospitals, Saveetha Institute of Medical and Technical Sciences, Saveetha University, Chennai, India

<sup>c</sup>Department of Chemical Engineering, Alagappa College of Technology, Anna University, Chennai 600 025, India

<sup>d</sup>Nanotechnology & Catalysis Research Centre, University of Malaya, Kuala Lumpur, 50603, Malaysia

 † Electronic supplementary information (ESI) available. See DOI: <https://doi.org/10.1039/d3ra02887a>

‡ These authors are equally contributed.



property. Leelavathi *et al.* reported ZnO@g-C<sub>3</sub>N<sub>4</sub> with anti-proliferative activity against human cervical cancer.<sup>22</sup> Curcumin has significant cancer-suppressive efficiency *in vitro* and *in vivo* against the progression of several cancers at all stages, including initiation, promotion, and propagation. Previous reports have demonstrated that curcumin-loaded ZnO nanoparticles show promising results against the rhabdomyosarcoma RD cell line.<sup>23</sup> A recent report investigated the cytotoxicity of the ZnO–curcumin nanodispersion against HT-29 cancer cells.<sup>24</sup> Yu Xia *et al.* reported the anticancer performance of curcumin-loaded-gelatin nanoparticles against MCF-7 cells.<sup>25</sup>

A heterogeneous composite of g-C<sub>3</sub>N<sub>4</sub> and ZnO NPs was reported to demonstrate significantly improved photoabsorption and catalytic activity.<sup>26</sup> Therefore, its synthesis has gained importance, and several methods of g-C<sub>3</sub>N<sub>4</sub>/ZnO composite synthesis have been introduced *viz.* two-step chemisorption method by Wang *et al.*,<sup>27</sup> ball milling method by Liu *et al.*,<sup>28</sup> calcination method by Zhu *et al.*,<sup>29</sup> reflux method by Wang *et al.*,<sup>30</sup> and reflux-vapour condensation method by Park *et al.*<sup>31</sup> Among them, the reflux and reflux-vapor condensation methods resulted in composites with superior architectures, namely the core–shell type g-C<sub>3</sub>N<sub>4</sub>/ZnO nanocomposite (for improved photoelectrocatalytic performance) and 1D nanorods-coated g-C<sub>3</sub>N<sub>4</sub> sheets at 0.12 mA cm<sup>-2</sup> photocurrent density, respectively.<sup>32,33</sup> It has been observed that the synthesis procedure plays a crucial role in the formation of well-established heterojunctions between the outer layers of ZnO NPs and the g-C<sub>3</sub>N<sub>4</sub> sheets, which in most cases contribute to the superior photocatalytic property.<sup>31</sup> Nevertheless, most of the synthesis procedures employed for the formation of g-C<sub>3</sub>N<sub>4</sub>/ZnO nanocomposites are not economically feasible, environment-friendly, and require multiple steps along with many by-products that are of no use. Considering all the issues associated with the formation of the g-C<sub>3</sub>N<sub>4</sub>/ZnO nanocomposite, we have attempted an *in situ* approach in this work toward the generation of ZnO NPs-embedded g-C<sub>3</sub>N<sub>4</sub> (g-C<sub>3</sub>N<sub>4</sub>@ZnO). The formed composite was studied thoroughly for physicochemical and surface properties using different characterization techniques. Further, the drug release kinetic models of the curcumin-loaded g-C<sub>3</sub>N<sub>4</sub>@ZnO (termed as g-C<sub>3</sub>N<sub>4</sub>@ZnO/C) nanocomposite were obtained by studying the changes over time at two different pH conditions (5 and 7.4). Finally, the biological activity of the g-C<sub>3</sub>N<sub>4</sub>@ZnO composite was evaluated by the *in vitro* cancer cell viability and lactate dehydrogenase (LDH) assays, in addition to antibacterial activity tests against two different bacterial cultures.

## 2. Experimental details

### 2.1 Materials and methods

Zinc acetate dihydrate (Zn(OAc)<sub>2</sub>·2H<sub>2</sub>O), melamine, sodium hydroxide (NaOH), and curcumin of analytical reagent (AR) grade were purchased from Sigma-Aldrich (Mumbai, India). The breast cancer cell line, MDA-MD-231, of human origin was obtained from National Centre for Cell Science (NCCS), Pune, India. Dulbecco's Modified Eagle Medium (DMEM), fetal bovine serum (FBS), trypsin–EDTA, 3-(4,5-dimethylthiazol-2-yl)-2,5-

diphenyltetrazolium bromide (MTT), dimethyl sulphoxide (DMSO), sodium bicarbonate, sodium pyruvate, nicotinamide adenine dinucleotide (NADH), and the penicillin–streptomycin (Pen–Strep) antibiotic solution were purchased from Hi-Media Laboratories (Mumbai, India).

### 2.2 Fabrication of g-C<sub>3</sub>N<sub>4</sub>@ZnO nanocomposite

For the preparation of the g-C<sub>3</sub>N<sub>4</sub>@ZnO nanocomposite by an *in situ* route, 50 mL of a 1 M zinc acetate dihydrate solution was added to 1 g melamine first, followed by 50 mL of a 2 M NaOH solution in a dropwise manner. The solution mixture was stirred continuously until a high amount of white slurry was observed, indicating melamine–zinc hydroxide mixture formation. Stirring was continued for another 18 h, and then, the precipitate was filtered, washed several times with distilled water, and centrifuged to obtain the ZnO NPs as the product. The obtained ZnO NPs were dried in a hot air oven maintained at 100 °C in order to remove the moisture/water, ground to a fine powder, and finally sintered at 550 °C (at a 5 °C min<sup>-1</sup> heating rate). The idea of increasing the sintering temperature to 550 °C is based on the fact that melamine undergoes a polycondensation reaction at this stage to form g-C<sub>3</sub>N<sub>4</sub>, and at the same time, the intermediate zinc hydroxide gets converted into ZnO NPs, further allowing the *in situ* generation of g-C<sub>3</sub>N<sub>4</sub>@ZnO.

### 2.3 Drug loading

For loading curcumin (drug) in g-C<sub>3</sub>N<sub>4</sub>@ZnO, we started with a formulation consisting of the carrier (g-C<sub>3</sub>N<sub>4</sub>@ZnO) and the drug at a weight ratio of 90 : 10; this sample was prepared by stirring the drug and carrier in the ethanol solvent for 1 h, and the solvent was removed by vacuum drying to obtain curcumin-loaded g-C<sub>3</sub>N<sub>4</sub>@ZnO (g-C<sub>3</sub>N<sub>4</sub>@ZnO/C) as the final product. To investigate the drug loading efficiency of g-C<sub>3</sub>N<sub>4</sub>@ZnO, 1 g of g-C<sub>3</sub>N<sub>4</sub>@ZnO/C in the dried form was dispersed in 200 mL of PBS (phosphate-buffered saline; pH 7.4), and absorbance was recorded at the absorption wavelength of 418 nm as a function of time using a UV-visible spectrophotometer.

### 2.4 Studies of curcumin drug release

The drug release kinetics was studied at two different physiological pH values 7.4 and 5 using the same UV-visible spectrophotometer set at an absorption wavelength of 418 nm. For the analysis, 1 g of g-C<sub>3</sub>N<sub>4</sub>@ZnO/C dispersed in 200 mL of PBS was placed on a shaking incubator at a temperature of 37 °C, and the shaking velocity was maintained at 100 rpm. At each specified time interval, about 1 mL of PBS solution was removed and replaced with fresh medium before the optical dispersion (OD) was recorded. The calibration plot was used to estimate the concentration of curcumin released into the buffer solution. The data shown indicate the mean ± SD (standard deviation) of three individual experiments.

### 2.5 Studies of antimicrobial activity

The antimicrobial activity assay for the g-C<sub>3</sub>N<sub>4</sub>@ZnO/C composite was performed against two different bacterial



cultures, namely Gram-positive *Staphylococcus aureus* (*S. aureus*) and Gram-negative *Escherichia coli* (*E. coli*), using the agar diffusion method. For the test, the cultures were first grown overnight, and the inoculum sizes were adjusted to 0.5 using the McFarland standard. This inoculum was spread in all directions on the agar plate using a fresh-sterile swab and then subjected to room-temperature drying. The next step involved making some punctures in the agar gel using a sterile puncturing tool followed by the addition of discs containing the tested sample ( $g\text{-C}_3\text{N}_4@ZnO/C$ ) at various concentrations on the agar medium with the help of sterile forceps. In this study, 30 mg mL<sup>-1</sup> each of chloramphenicol and amoxycillin were selected as the positive controls for the microbial cultures of *S. aureus* and *E. coli*, respectively. All the cultures were incubated for a 24 h period at 37 °C, and at the incubation time, the diameter of the zone of inhibition (ZOI) and minimum inhibitory concentration (MIC) were recorded. The ZOI and MIC of  $g\text{-C}_3\text{N}_4@ZnO/C$  correspond to growth inhibition at a specified concentration and the lowest concentration that can inhibit the visible growth of the bacterial strain, respectively.

## 2.6 *In vitro* cancer cell viability assay

To investigate the anticancer activity of the  $g\text{-C}_3\text{N}_4@ZnO/C$  composite, *in vitro* cell viability studies were performed using the MTT assay using MDA-MB-231 human adenocarcinoma cells. Briefly, the cells were first seeded at a volume of  $5 \times 10^3$  cells per mL in 96-well plates and were allowed to grow in a growth medium (DMEM supplemented with 10% FBS and 1% Pen-Strep solution) under 5% CO<sub>2</sub> and 95% O<sub>2</sub> at 37 °C. At the

end of a 24 h incubation period, the cell medium was removed; the cells were washed with PBS two times, and fresh medium containing different concentrations (1, 5, 50, 100, 250 μg mL<sup>-1</sup>) of the  $g\text{-C}_3\text{N}_4@ZnO/C$  composite was added. Similarly, after incubation for 24 h, the sample-treated cells were subjected to medium removal two times PBS wash, and the addition of fresh medium containing 10 μL of the MTT reagent. After incubation for another 3 h, the supernatant was decanted from each well; 100 μL DMSO was added so as to dissolve the formazan crystals, if formed, by gently pipetting 2–3 times and finally, the absorbance at 570 nm was measured using a microplate reader. The following eqn (1) was used to calculate the growth inhibition rate of the  $g\text{-C}_3\text{N}_4@ZnO/C$  composite.

$$\text{Viability of the cells(\%)} = \frac{A_{570 \text{ nm}} \text{ of treated cells}}{A_{570 \text{ nm}} \text{ of control cells}} \times 100 \quad (1)$$

## 2.7 Lactate dehydrogenase (LDH) activity assay

The mechanistic action of the  $g\text{-C}_3\text{N}_4@ZnO/C$  composite in the MDA-MB-231 cancer cells was investigated by measuring the extent of LDH released from the cells following sample treatment. Similar to the cell viability assay, the MDA-MB-231 cells ( $1 \times 10^5$  cells per well) in a 96-well plate were treated with different concentrations of the  $g\text{-C}_3\text{N}_4@ZnO/C$  composite (1–250 g mL<sup>-1</sup>) for a 24 h period. At the end of incubation, the cell medium was collected, centrifuged for 10 min at 5000 rpm, and the pellet obtained was dissolved in a solution mixture consisting of 100 μL culture media, 100 μL sodium pyruvate (2.5 mg mL<sup>-1</sup> of

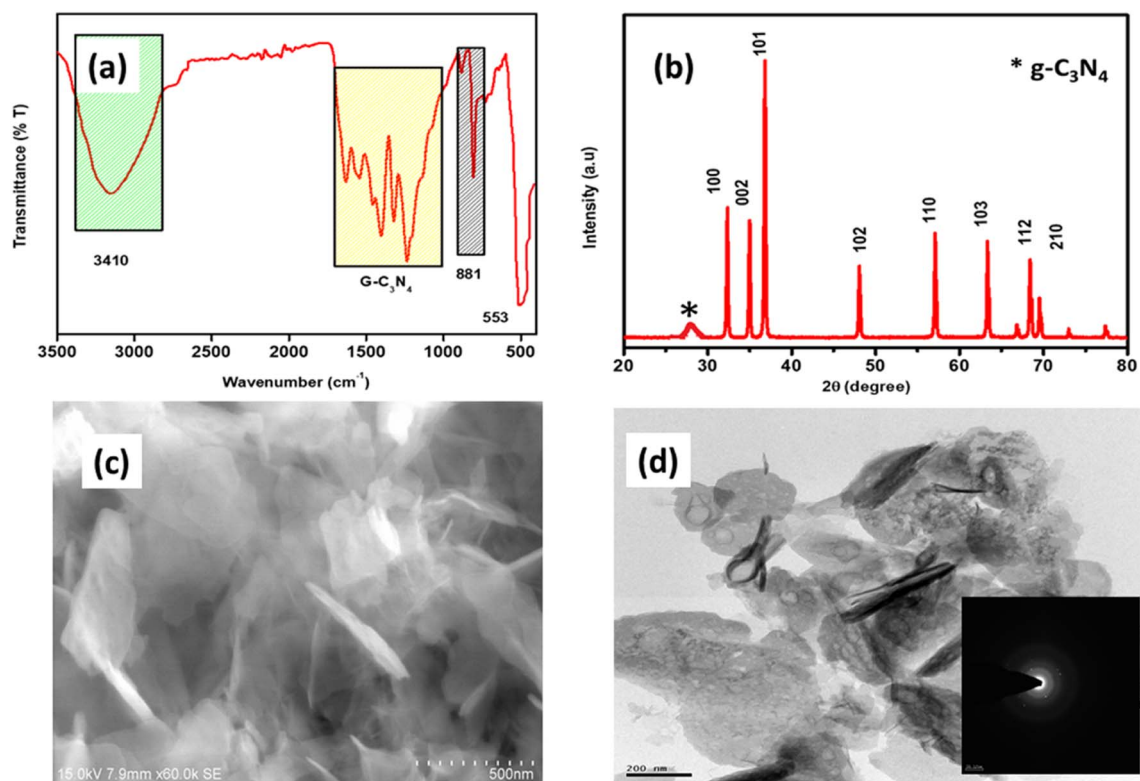


Fig. 1 (a) The FTIR spectrum, (b) XRD pattern, (c) SEM, and (d) HRTEM analysis of the  $g\text{-C}_3\text{N}_4@ZnO$  nanocomposite.



PBS), and 100  $\mu\text{L}$  reduced NADH ( $2.5 \text{ mg mL}^{-1}$  of PBS) and made up to a total volume of 3 mL using the 0.1 M potassium phosphate buffer (pH 7.4). Finally, the LDH content ( $\text{IU L}^{-1}$ ) in the culture medium was quantified by recording the speed of NADH oxidation at 340 nm for 3 min at 30 s intervals using a Shimadzu UV-vis spectrophotometer.

### 3. Results and discussion

Fig. 1(a) shows the Fourier Transform-Infra Red (FT-IR) spectrum, which reveals the functional groups of the  $g\text{-C}_3\text{N}_4@\text{ZnO}$  composite. The characteristic peaks observed at 1637 and 1243  $\text{cm}^{-1}$  can be linked to the C=N and C-N stretching vibrations originating from the  $g\text{-C}_3\text{N}_4$  molecules,<sup>31</sup> while the in-plane bending vibration was observed at 881  $\text{cm}^{-1}$ .<sup>29</sup> Moreover, the additional peaks related to the individual components of ZnO and  $g\text{-C}_3\text{N}_4$  are attributed to the successful formation of the  $g\text{-C}_3\text{N}_4/\text{ZnO}$  composite. Similarly, the powder X-ray diffraction (XRD) pattern of the  $g\text{-C}_3\text{N}_4@\text{ZnO}$  composite shown in Fig. 1(b)

represents the distinct peaks of  $g\text{-C}_3\text{N}_4$  at  $2\theta = 27.4^\circ$  corresponding to the (100) diffraction plane, confirming the in-plane packing motif, while the other peak at  $35^\circ$  (002) confirms the stacking structure.<sup>34</sup> The appearance of a single peak related to the  $g\text{-C}_3\text{N}_4$  compound indicates that no impurities or by-products were formed during the synthesis process. In addition, the observation of distinct diffraction peaks for the ZnO compound is in good agreement with the JCPDS data 79-2205 and corresponds with the hexagonal structure, while the orderly arrangement of the peaks supports the high crystalline nature of ZnO. Hence, the X-ray crystalline diffraction data confirmed the formation of the  $g\text{-C}_3\text{N}_4@\text{ZnO}$  composite in a highly crystalline form with very high purity. The scanning electron microscopy (SEM) and high-resolution transmission electron microscopy (HR-TEM) analyses of the  $g\text{-C}_3\text{N}_4@\text{ZnO}$  nanocomposite depicted in Fig. 1(c) and (d), respectively, indicate that the morphology of the  $g\text{-C}_3\text{N}_4$  and ZnO components appeared as sheets and rod-shaped, respectively. These structures also suggest that the ZnO nanorods were embedded

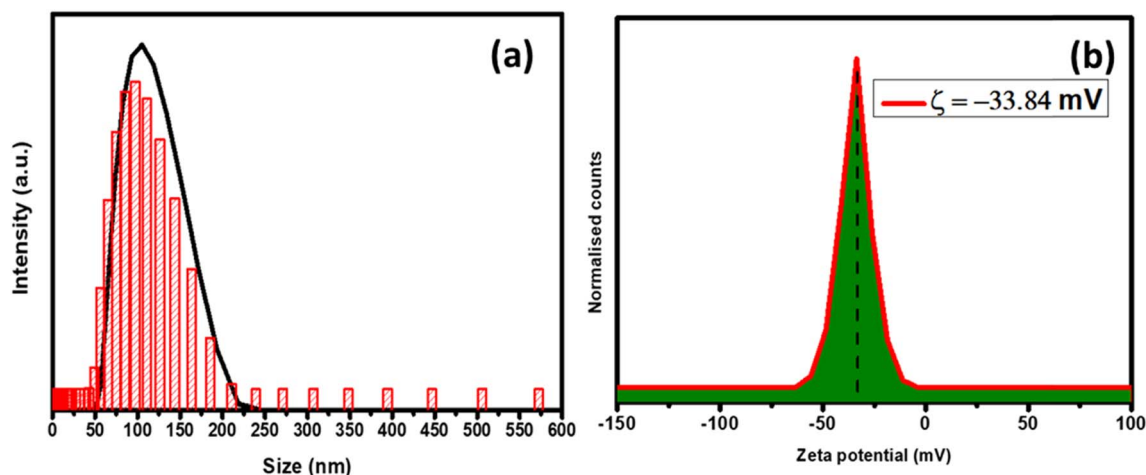


Fig. 2 (a) The particle size analysis and (b) the zeta potential pattern of the  $g\text{-C}_3\text{N}_4@\text{ZnO}$  nanocomposite.

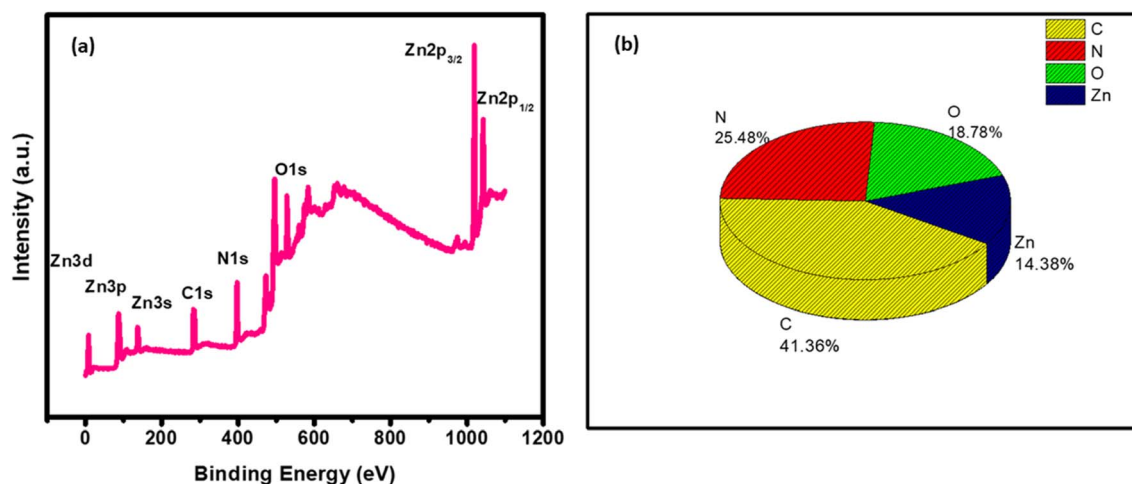


Fig. 3 (a) The XPS survey spectrum and (b) percentage elemental composition of  $g\text{-C}_3\text{N}_4@\text{ZnO}$ .



within the  $g\text{-C}_3\text{N}_4$  sheets, as visible in Fig. 1(c). Moreover, the HR-TEM image of ZnO provided in Fig. 1(d) represents the characteristic rod-shaped morphology corresponding to the hexagonal crystalline plane (001) (as indicated by the SAED pattern shown in the inset).<sup>34</sup> Further, the HRTEM analysis of  $g\text{-C}_3\text{N}_4@ZnO$  confirmed the successful embedding of the ZnO nanorods inside the  $g\text{-C}_3\text{N}_4$  sheets.

Fig. 2(a) and (b) provide the particle size distribution and zeta potential studies of the  $g\text{-C}_3\text{N}_4@ZnO$  nanocomposite, respectively. The particle size distribution analysis indicates that  $g\text{-C}_3\text{N}_4@ZnO$  in the solution phase was within the nanometre size range *i.e.*, the average particle size was around 122 nm (Fig. 2(a)). Further, the zeta potential measurements provided in Fig. 2(b) confirm the negative surface charges of the  $g\text{-C}_3\text{N}_4@ZnO$  composite with a value of  $-33.84$  mV.

The X-ray photoelectron spectroscopy (XPS) analysis was performed to investigate the elemental composition of the  $g\text{-C}_3\text{N}_4/ZnO$  composite (a representative of heterojunctions), and the results are shown in Fig. 3(a) and (b). Fig. 3(a) represents the XPS analysis, wherein all the elements present in the composite, including Zn, O, C, and N, are seen as analysed by the CASA software. Moreover, the percentage elemental composition is shown in Fig. 3(b).

Similarly, in the XPS analysis of the surface species of the  $g\text{-C}_3\text{N}_4@ZnO$  sample, as shown in Fig. 4(a–d), the C 1s spectrum presented two different peaks at 284.9 and 288.2 eV corresponding to the surface adventitious C and  $sp^2$ -bonded C in the

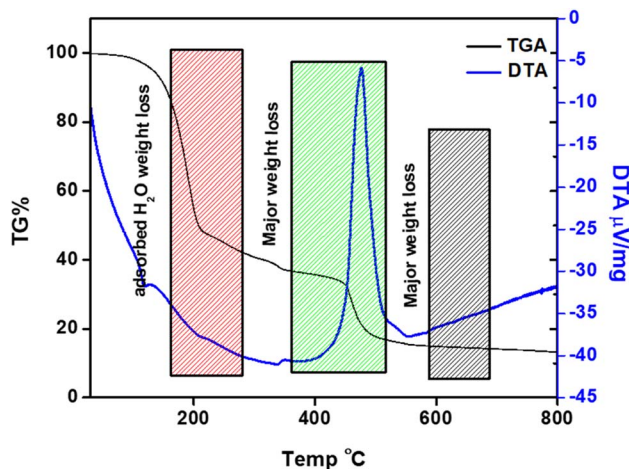


Fig. 5 Comparison of the TGA and DTA profiles of the  $g\text{-C}_3\text{N}_4@ZnO$  composite.

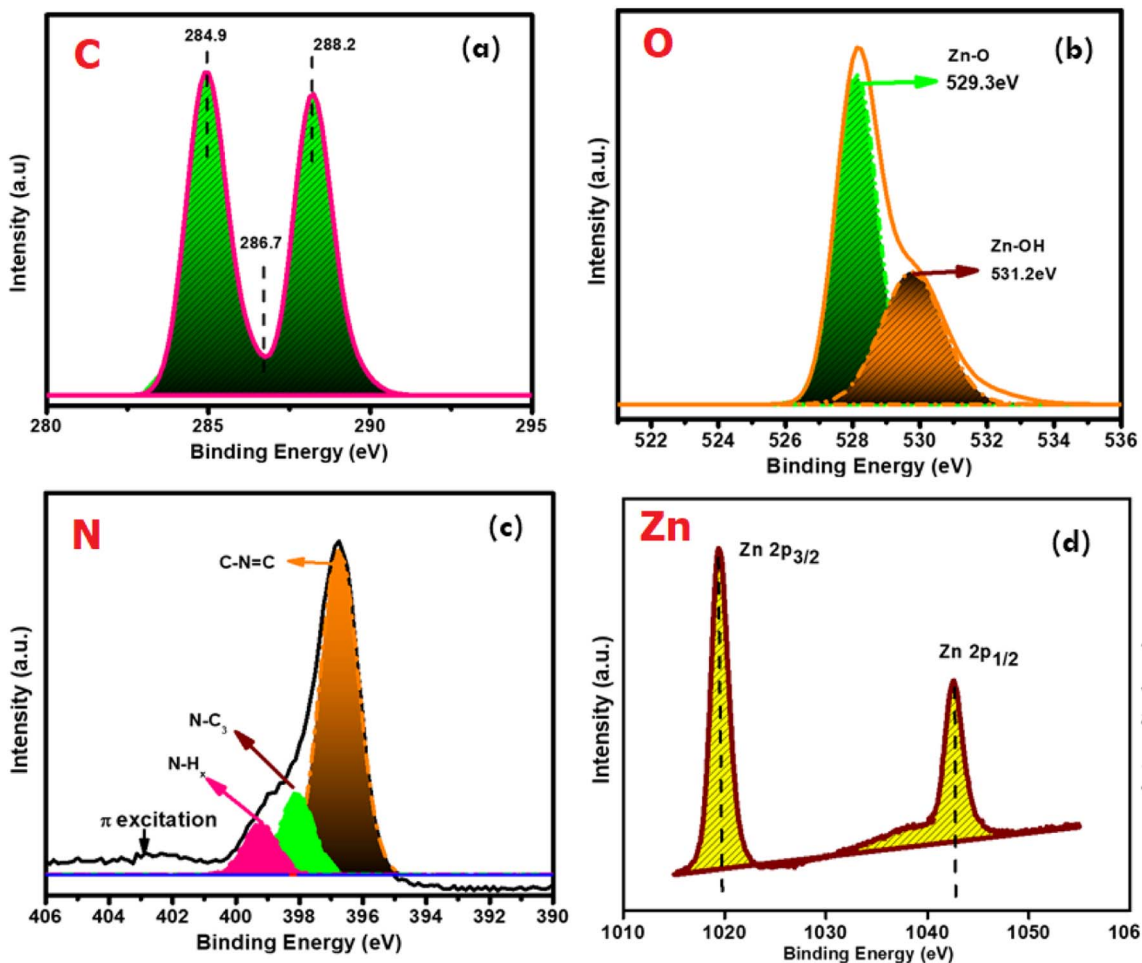


Fig. 4 The deconvoluted spectra of the elements (a) C, (b) O, (c) N, and (d) Zn present in the  $g\text{-C}_3\text{N}_4@ZnO$  sample.



N=C-N coordination bond, respectively (Fig. 4(a)).<sup>35</sup> Further, in the O 1s spectrum (Fig. 4(b)), the peaks observed at 531.2 and 529.3 eV can be attributed to chemisorbed (OC) oxygen, oxygen

from the deficient regions (OV), and the O<sub>2</sub><sup>2-</sup> species in the lattice (OL).<sup>33</sup> Based on the observation of the O peak at 529.3 eV related to the chemisorbed oxygen species, it can be inferred

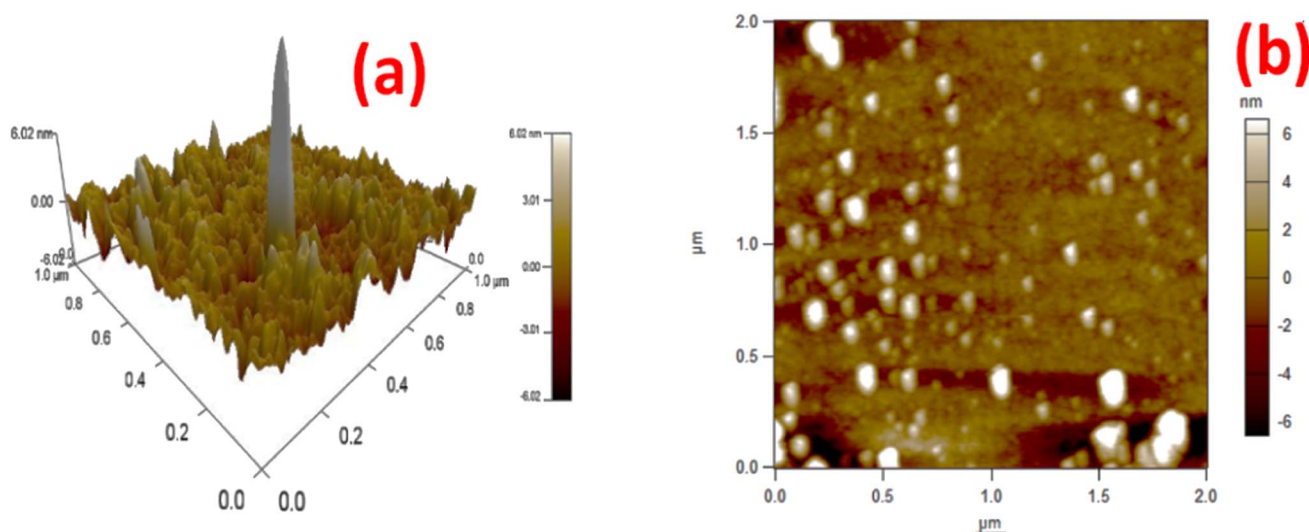


Fig. 6 The AFM topography of the g-C<sub>3</sub>N<sub>4</sub>@ZnO composite (a) 3D and (b) 2D images.

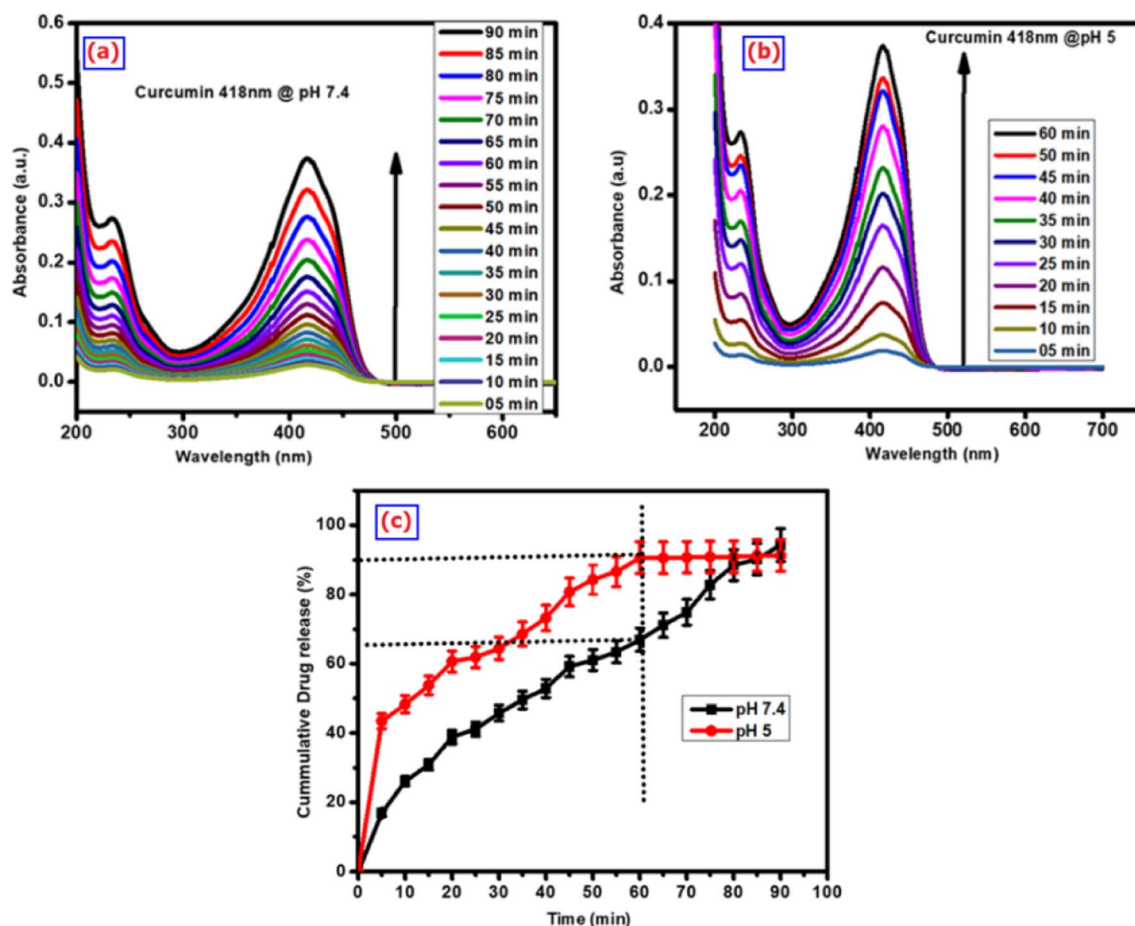


Fig. 7 The UV-vis spectroscopic analysis of curcumin drug released from the g-C<sub>3</sub>N<sub>4</sub>@ZnO/C composite at pH (a) pH 7.4 and (b) 5; (c) the corresponding curcumin drug release kinetics from the composite at pH 7.4 and 5.



that this element is associated with the high-level surface defects in the g-C<sub>3</sub>N<sub>4</sub>/ZnO nanocomposite, while the other peak at 531.2 eV is from the surface hydroxyl functional groups.<sup>34</sup> Similarly, the N and Zn spectra shown in Fig. 4(c) and (d) confirm the presence of the respective elements in the composite; the characteristic peaks of Zn appearing at 1020.0 and 1042.0 eV can be linked to Zn 2p<sub>3/2</sub> and 2p<sub>1/2</sub>, respectively. Further, the observation of a positive shift for the O 1s binding energy position and the negative shift of the Zn 2p peaks suggest the possible chemical bond formation between the ZnO and g-C<sub>3</sub>N<sub>4</sub> components in the composite.

The comparison of the thermogravimetric analysis (TGA) and differential thermal analysis (DTA) studies of the g-C<sub>3</sub>N<sub>4</sub>/ZnO composite is provided in Fig. 5. Weight loss in the spectrum is categorized into three different regions comprising minor weight loss, significant weight loss, and the residual mass. In the graph, a minor weight loss is observed at around 180 °C, which is linked to the loss of adsorbed water molecules, moisture, or hydroxyl groups. The significant weight loss of the composite at around 450 °C can be linked to the phase change of melamine into g-C<sub>3</sub>N<sub>4</sub>. In the same way, the significant weight loss around 550 °C may be due to the degradation of the g-C<sub>3</sub>N<sub>4</sub> layer in the g-C<sub>3</sub>N<sub>4</sub>@ZnO composite.<sup>36</sup>

The atomic force microscopic (AFM) studies provided the topological analysis of the g-C<sub>3</sub>N<sub>4</sub>@ZnO composite. In Fig. 6(a) and (b), the top view of the ZnO@g-C<sub>3</sub>N<sub>4</sub> sample shows a well-organized homogenous pattern. In addition, the analysis indicated that the nanorods of ZnO were immobilized inside the layers of g-C<sub>3</sub>N<sub>4</sub>, and thus, the results are in good agreement with the HRTEM analysis (Fig. 1(d)).

The release of curcumin from the composite of g-C<sub>3</sub>N<sub>4</sub>@ZnO at pH 7.4 (neutral) and 5 (slightly acidic) are compared in Fig. 7(a) and (b), while the release kinetics are presented in Fig. 7(c). From the analysis, it could be observed that the composite released 90% of the loaded drug at the acidic pH of 5 in the first 60 min; however, at the neutral pH of 7.4, the drug release from the composite was around 66%. This difference in release pattern is due to the enhanced interaction of protons in the acidic medium, which allows the g-C<sub>3</sub>N<sub>4</sub> groups to open up the cavities/pores easily to mediate the release of curcumin.

The antibacterial activity of the g-C<sub>3</sub>N<sub>4</sub>@ZnO/C composite against the bacterial cultures of *E. coli* and *S. aureus* at different drug concentrations between 25 and 100 mg mL<sup>-1</sup> is shown in Fig. 8(i) and (ii). It can be observed from the figure that the composite exhibited significant levels of antibacterial activity against both cultures, and this activity increased with an increase in concentration. Such activity of the composite is due to the presence of Zn<sup>2+</sup> and curcumin in the composite, *i.e.*, the interaction of Zn<sup>2+</sup> with the cell wall results in the depletion of the cell membrane, causing the release of the intracellular fluids, which is associated with loss of viability. Additionally, the curcumin drug also interacts with the physiological pathways of the cells, disrupts the normal mechanisms and eventually leads to bacterial cell death (Table 1).

The cell viability and proliferation studies of the g-C<sub>3</sub>N<sub>4</sub>@ZnO/C composite were carried out by the MTT assay, *i.e.* the cells were treated with different concentrations of the drug (1 to 250 µg mL<sup>-1</sup>) and for 7 consecutive days (day 1–7), and the results are shown in Fig. 9(i) and (ii), respectively. In the concentration- and time-dependent cell viability studies, the reduction in cell viability was significant at 250 µg mL<sup>-1</sup> (day 1). As the concentration increased, the reduction in viable cells was also enhanced. Further, the microscopic images of the treated cells shown in Fig. 9(iii) indicate decreased cell viability levels over different periods and concentrations. The mechanism of action of the drug from the nanocomposite is given in the ESI section (Fig. S1)† along with the confocal images of (a) control, (b) g-C<sub>3</sub>N<sub>4</sub>@ZnO, (C) curcumin, and (d) g-C<sub>3</sub>N<sub>4</sub>@ZnO/curcumin, as well as (d) cell viability at 24 h (Fig. S2)†. In the confocal microscopy images, we could see curcumin inside the MDA-MD-231 cells. The cell viability results showed that the

Table 1 The ZOI of g-C<sub>3</sub>N<sub>4</sub>@ZnO/C against (i) *E. coli* and (ii) *S. aureus*. a, b, c, d, and S correspond to the testing sample concentrations 25, 50, 75, and 100 mg mL<sup>-1</sup> and control, respectively

Microorganisms	Zone of inhibition (mm)				
	a	b	c	d	S
<i>Staphylococcus aureus</i>	8	9	11	13	13
<i>Escherichia coli</i>	8	10	12	14	12

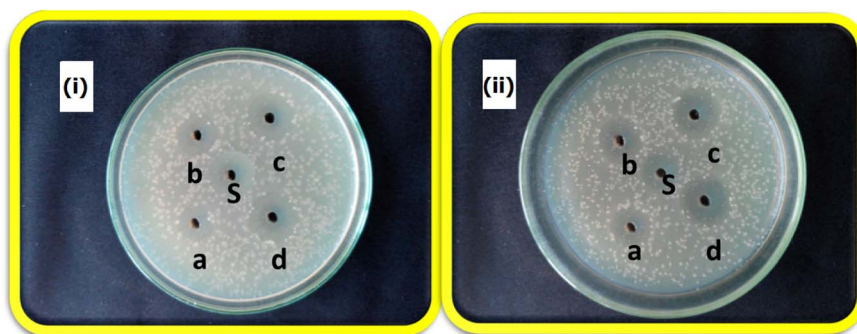


Fig. 8 The antibacterial activity of g-C<sub>3</sub>N<sub>4</sub>@ZnO/C against (i) *E. coli* and (ii) *S. aureus*. a, b, c, d, and S correspond to the testing sample concentrations 25, 50, 75, and 100 mg mL<sup>-1</sup> and control, respectively.



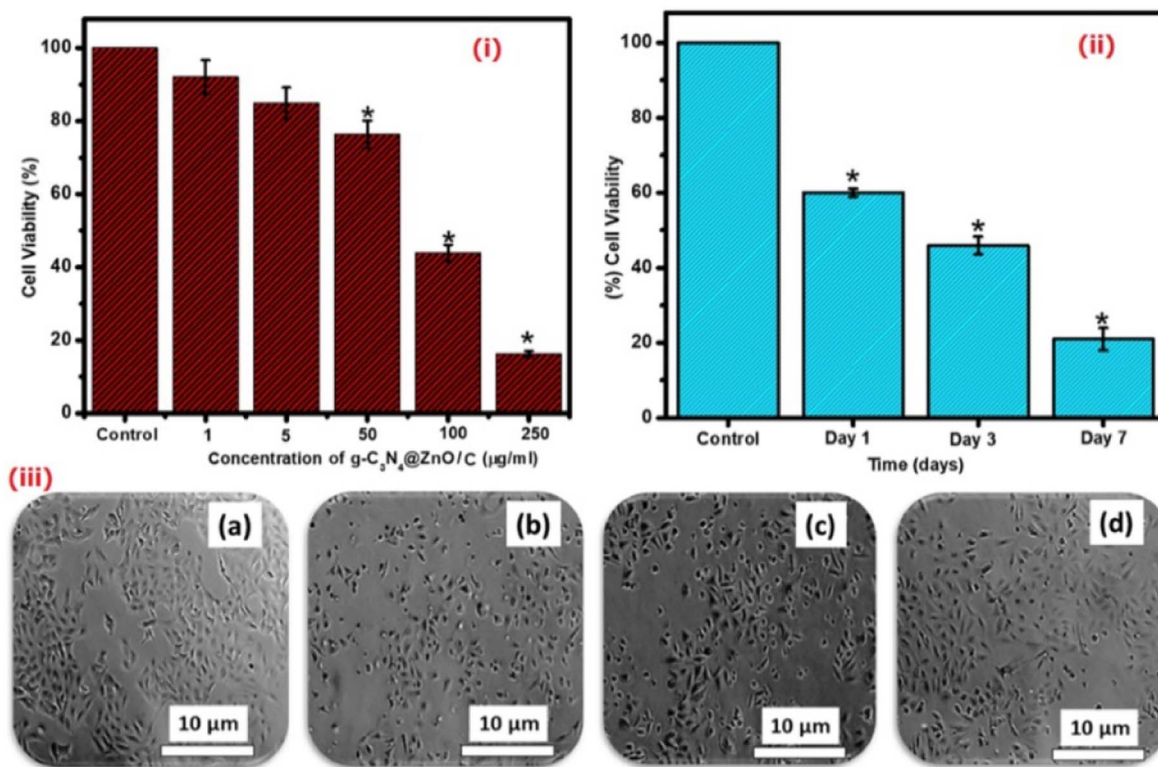


Fig. 9 The *in vitro* cell viability and proliferation studies of MDA-MD-231 cells treated with the g-C<sub>3</sub>N<sub>4</sub>@ZnO/C sample at different (i) concentrations and (ii) treatment periods, as evaluated by the MTT assay. (iii) The cell morphology of MDA-MD-231 cells treated with g-C<sub>3</sub>N<sub>4</sub>@ZnO/C at the IC<sub>50</sub> of 94 µg mL<sup>-1</sup>, as photographed using a simple microscope: (a) control, (b) day 1, (c) day 3, and (d) day 7.

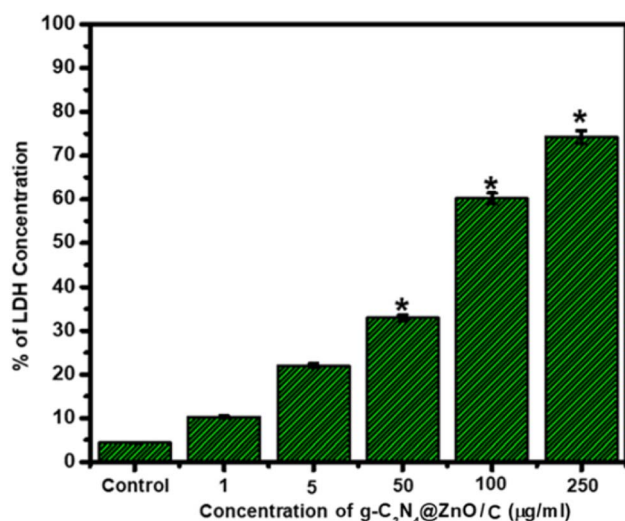


Fig. 10 Variations in LDH (%) release from MDA-MD-231 cells treated with the g-C<sub>3</sub>N<sub>4</sub>@ZnO/C sample at different concentrations up to 250 µg mL<sup>-1</sup>.

minimum cell viability (%) was observed in g-C<sub>3</sub>N<sub>4</sub>@ZnO/C curcumin nanocomposite, indicating its effective performance against MDA-MD-231 cells.

The reduction in cell viability followed by treatment with the C<sub>3</sub>N<sub>4</sub>@ZnO/C sample presents preliminary evidence for the

anticancer activity of the formulation and can be attributed to the presence of Zn metal and the medicinal properties of curcumin.

The cytotoxic mechanism of the g-C<sub>3</sub>N<sub>4</sub>@ZnO/C composite was determined using the LDH-colorimetric assay, as shown in Fig. 10. The assay is dependent on the cytoplasmic LDH enzyme-catalyzed oxidation of lactate to pyruvate and *vice versa* as LDH is a known marker for understanding membrane integrity and also a regulator of vital biochemical reactions.<sup>37,38</sup> From the graph, it is clear that the g-C<sub>3</sub>N<sub>4</sub>@ZnO/C-treated cells released LDH, which increased with drug concentration. LDH released from the plasma damages the cell membrane, causes shrinkage of the cytoplasm, and cleaves the DNA into smaller fragments.<sup>39,40</sup> A significant increase in the release of LDH from the cells was observed at concentrations above 50 µg mL<sup>-1</sup>, and at the highest concentration 250 µg mL<sup>-1</sup>, LDH release was around 78% compared with the control sample. Therefore, g-C<sub>3</sub>N<sub>4</sub>@ZnO/C shows significant levels of toxicity to the cancer cells, and thus, the composite can be a potential platform for the treatment of tumour cells.

## 4. Conclusion

In summary, we indicate the successful fabrication of the g-C<sub>3</sub>N<sub>4</sub>@ZnO composite using an *in situ* fabrication process followed by the efficient loading of curcumin drug into the composite. On testing the composite, the FT-IR analysis showed the conjugation of the g-C<sub>3</sub>N<sub>4</sub> groups with ZnO, while the



crystallinity of the composite was determined by XRD. The HRTEM analysis confirmed the rod-shaped morphology of the particles, which were partially wrapped in the sheets of g-C<sub>3</sub>N<sub>4</sub>. Moreover, the elements present in the composite were analyzed using XPS, which confirmed the presence of C, N, Zn, and O and thereby verified the successful formation of the g-C<sub>3</sub>N<sub>4</sub>/ZnO composite. The drug release profiles of curcumin at two different pHs indicated that the acidic pH 5 is more suitable for sustainable drug release. The biological evaluation of the g-C<sub>3</sub>N<sub>4</sub>@ZnO/C sample supported its significant antibacterial activity against *E. coli* and *S. aureus* in addition to the anticancer action against the MDA-MB-231 cancer cells, demonstrating a very low IC<sub>50</sub> value of 94 μg mL<sup>-1</sup> at 24 h. This composite is the first to be prepared by an *in situ* method and used for treatment against MDA-MB-231 cells. From the SEM, TEM and AFM analyses, we confirmed that the ZnO nanoparticles were embedded in the 2D stacked layers of g-C<sub>3</sub>N<sub>4</sub>. Usually, a two-step process is employed for preparing this composite. We have adopted a single-step process, and ZnO growth on the layers of g-C<sub>3</sub>N<sub>4</sub> is clearly visible from the morphological analysis. In this work, we have achieved the embedding of nanoparticles with a rod-like morphology on a layered structure. The rod-like morphology serves as a good tool for sustained drug delivery. Further observation of LDH activity indicated that the mechanistic action of g-C<sub>3</sub>N<sub>4</sub>@ZnO/C is mediated by the presence of Zn and curcumin drug, thereby providing preliminary evidence that this drug-loaded nanocomposite can be an ideal candidate for treating breast cancer cells.

## Conflicts of interest

There is no conflict of interest with this work.

## Acknowledgements

One of the authors Varun Prasath Padmanabhan would like to acknowledge the financial support from Council of Scientific and Industrial Research (CSIR), Government of India, for the Research Associate Fellowships (09/115(0793)/2020 EMR-I).

## References

- 1 E. C. Dreaden, A. M. Alkilany, X. Huang, C. J. Murphy and M. A. El-Sayed, The golden age: gold nanoparticles for biomedicine, *Chem. Soc. Rev.*, 2012, **41**(7), 2740–2779.
- 2 C. M. Cobley, J. Chen, E. C. Cho, L. V. Wang and Y. Xia., Gold nanostructures: a class of multifunctional materials for biomedical applications, *Chem. Soc. Rev.*, 2011, **40**(1), 44–56.
- 3 X.-d. Wang, T.-y. Zhou, X.-h. Song, Y. Jiang, C. J. Yang and X. Chen, Chameleon clothes for quantitative oxygen imaging, *J. Mater. Chem.*, 2011, **21**(44), 17651–17653.
- 4 K. Yang, L. Feng, X. Shi and Z. Liu, Nano-graphene in biomedicine: theranostic applications, *Chem. Soc. Rev.*, 2013, **42**(2), 530–547.
- 5 X. Cai, H. Dong, J. Ma, H. Zhu, W. Wu, M. Chu, Y. Li and D. Shi, Effects of spatial distribution of the nuclear localization sequence on gene transfection in cationic-polyplexes, *J. Mater. Chem. B*, 2013, **1**(12), 1712–1721.
- 6 K. P. Loh, Q. Bao, G. Eda and M. Chhowalla, Graphene oxide as a chemically tunable platform for optical applications, *Nat. Chem.*, 2010, **2**(12), 1015.
- 7 X. Chen, B. Su, G. Wu, C. J. Yang, Z. Zhuang, X. Wang and X. Chen, Platinum nanoflowers supported on graphene oxide nanosheets: their green synthesis, growth mechanism, and advanced electrocatalytic properties for methanol oxidation, *J. Mater. Chem.*, 2012, **22**(22), 11284–11289.
- 8 L. Feng, L. Wu and X. Qu, New horizons for diagnostics and therapeutic applications of graphene and graphene oxide, *Adv. Mater.*, 2013, **25**(2), 168–186.
- 9 C.-H. Lu, H.-H. Yang, C.-L. Zhu, X. Chen and G.-N. Chen, A graphene platform for sensing biomolecules, *Angew. Chem.*, 2009, **121**(26), 4879–4881.
- 10 S. He, B. Song, D. Li, C. Zhu, W. Qi, Y. Wen, L. Wang, S. Song, H. Fang and C. Fan, A graphene nanoprobe for rapid, sensitive, and multicolor fluorescent DNA analysis, *Adv. Funct. Mater.*, 2010, **20**(3), 453–459.
- 11 Q. Liu, B. Guo, Z. Rao, B. Zhang and J. R. Gong, Strong two-photon-induced fluorescence from photostable, biocompatible nitrogen-doped graphene quantum dots for cellular and deep-tissue imaging, *Nano Lett.*, 2013, **13**(6), 2436–2441.
- 12 Z. Liu, J. T. Robinson, X. Sun and H. Dai, PEGylated nanographene oxide for delivery of water-insoluble cancer drugs, *J. Am. Chem. Soc.*, 2008, **130**(33), 10876–10877.
- 13 B. Tian, C. Wang, S. Zhang, L. Feng and Z. Liu, Photothermally enhanced photodynamic therapy delivered by nano-graphene oxide, *ACS Nano*, 2011, **5**(9), 7000–7009.
- 14 P. Huang, J. Lin, X. Wang, Z. Wang, C. Zhang, M. He, K. Wang, *et al.*, Light-triggered theranostics based on photosensitizer-conjugated carbon dots for simultaneous enhanced-fluorescence imaging and photodynamic therapy, *Adv. Mater.*, 2012, **24**(37), 5104–5110.
- 15 J. T. Robinson, S. M. Tabakman, Y. Liang, H. Wang, H. S. Casalongue, D. Vinh and H. Dai, Ultrasmall reduced graphene oxide with high near-infrared absorbance for photothermal therapy, *J. Am. Chem. Soc.*, 2011, **133**(17), 6825–6831.
- 16 M. Li, L. Zhang, M. Wu, Y. Du, X. Fan, M. Wang, L. Zhang, Q. Kong and J. Shi, Mesoporous CeO<sub>2</sub>/g-C<sub>3</sub>N<sub>4</sub> nanocomposites: remarkably enhanced photocatalytic activity for CO<sub>2</sub> reduction by mutual component activations, *Nano Energy*, 2016, **19**, 145–155.
- 17 J. Tian, L. Zhang, M. Wang, X. Jin, Y. Zhou, J. Liu and J. Shi, Remarkably enhanced H<sub>2</sub> evolution activity of oxidized graphitic carbon nitride by an extremely facile K<sub>2</sub>CO<sub>3</sub>-activation approach, *Appl. Catal., B*, 2018, **232**, 322–329.
- 18 S. Cao, J. Low, J. Yu and M. Jaroniec, Polymeric photocatalysts based on graphitic carbon nitride, *Adv. Mater.*, 2015, **27**(13), 2150–2176.
- 19 F. Su, S. C. Mathew, G. Lipner, X. Fu, M. Antonietti, S. Blechert and X. Wang, mpg-C<sub>3</sub>N<sub>4</sub>-catalyzed selective oxidation of alcohols using O<sub>2</sub> and visible light, *J. Am. Chem. Soc.*, 2010, **132**(46), 16299–16301.



- 20 Y. Zhang, M. Li, X. Gao, Y. Chen and T. Liu, Nanotechnology in cancer diagnosis: progress, challenges and opportunities, *J. Hematol. Oncol.*, 2019, **12**, 1–13.
- 21 C. Maksoudian, N. Saffarzadeh, E. Hesemans, N. Dekoning, K. Buttiens and S. J. Soenen, Role of inorganic nanoparticle degradation in cancer therapy, *Nanoscale Adv.*, 2020, **2**, 3734–3763.
- 22 H. Leelavathi, R. Arulmozhi, R. Muralidharan, N. Abirami, S. Tamizharasan and A. Kumarasamy, Exploration of ZnO decorated g-C<sub>3</sub>N<sub>4</sub> amphiphilic anticancer drugs for antiproliferative activity against human cervical cancer, *J. Drug Deliv. Sci. Technol.*, 2022, **22**, 103126.
- 23 W. P. T. D. Perera, R. K. Dissanayake, U. I. Ranatunga, N. M. Hettiarachchi, K. D. C. Perera, J. M. Unagolla, R. T. De Silva and L. R. Pahalagedar, Curcumin loaded zinc oxide nanoparticles for activity-enhanced antibacterial and anticancer applications, *RSC Adv.*, 2020, **10**, 30785–30795.
- 24 Z. Sayyar, H. Jafarizadeh-Malmiri and N. Beheshtizadeh, A study on the anticancer and antimicrobial activity of curcumin nanodispersion and synthesized ZnO nanoparticles, *Process Biochem.*, 2022, **121**, 18–25.
- 25 Y. Xia, R. Xu, S. Ye, J. Yan, P. Kumar, P. Zhang and X. Zhao, Microfluidic Formulation of Curcumin-Loaded Multiresponsive Gelatin Nanoparticles for Anticancer Therapy, *ACS Biomater. Sci. Eng.*, 2023, **9**, 3402–3413.
- 26 X. Yuan, S. Duan, G. Wu, L. Sun, G. Cao, D. Li, H. Xu, Q. Li and D. Xia, Enhanced catalytic ozonation performance of highly stabilized mesoporous ZnO doped g-C<sub>3</sub>N<sub>4</sub> composite for efficient water decontamination, *Appl. Catal., A*, 2018, **551**, 129–138.
- 27 Y. Wang, R. Shi, J. Lin and Y. Zhu, Enhancement of photocurrent and photocatalytic activity of ZnO hybridized with graphite-like C<sub>3</sub>N<sub>4</sub>, *Energy Environ. Sci.*, 2011, **4**(8), 2922–2929.
- 28 W. Liu, M. Wang, C. Xu, S. Chen and X. Fu, Significantly enhanced visible-light photocatalytic activity of g-C<sub>3</sub>N<sub>4</sub> via ZnO modification and the mechanism study, *J. Mol. Catal. A: Chem.*, 2013, **368**, 9–15.
- 29 Y.-P. Zhu, M. Li, Y.-L. Liu, T.-Z. Ren and Z.-Y. Yuan, Carbon-doped ZnO hybridized homogeneously with graphitic carbon nitride nanocomposites for photocatalysis, *J. Phys. Chem. C*, 2014, **118**(20), 10963–10971.
- 30 J. Wang, Z. Yang, X. Gao, W. Yao, W. Wei, X. Chen, R. Zong and Y. Zhu, Core-shell g-C<sub>3</sub>N<sub>4</sub>@ ZnO composites as photoanodes with double synergistic effects for enhanced visible-light photoelectrocatalytic activities, *Appl. Catal., B*, 2017, **217**, 169–180.
- 31 T. J. Park, R. C. Pawar, S. Kang and C. S. Lee, Ultra-thin coating of gC 3 N 4 on an aligned ZnO nanorod film for rapid charge separation and improved photodegradation performance, *RSC Adv.*, 2016, **6**(92), 89944–89952.
- 32 Y. Wang, X. Liu, J. Liu, B. Han, X. Hu, F. Yang, Z. Xu, *et al.*, Carbon quantum dot implanted graphite carbon nitride nanotubes: excellent charge separation and enhanced photocatalytic hydrogen evolution, *Angew. Chem.*, 2018, **130**(20), 5867–5873.
- 33 W.-K. Jo and N. C. S. Selvam, Enhanced visible light-driven photocatalytic performance of ZnO–g-C<sub>3</sub>N<sub>4</sub> coupled with graphene oxide as a novel ternary nanocomposite, *J. Hazard. Mater.*, 2015, **299**, 462–470.
- 34 X. Wang, K. Maeda, A. Thomas, K. Takane, G. Xin, J. M. Carlsson, K. Domen and M. Antonietti, A metal-free polymeric photocatalyst for hydrogen production from water under visible light, *Nat. Mater.*, 2009, **8**(1), 76–80.
- 35 X. Zhang, J. Qin, Y. Xue, P. Yu, B. Zhang, L. Wang and R. Liu, Effect of aspect ratio and surface defects on the photocatalytic activity of ZnO nanorods, *Sci. Rep.*, 2014, **4**, 4596.
- 36 C. Chang, Y. Fu, M. Hu, C. Wang, G. Shan and L. Zhu, Photodegradation of bisphenol A by highly stable palladium-doped mesoporous graphite carbon nitride (Pd/mpg-C<sub>3</sub>N<sub>4</sub>) under simulated solar light irradiation, *Appl. Catal., B*, 2013, **142**, 553–560.
- 37 J. H. Zheng, Q. Jiang and J. S. Lian, Synthesis and optical properties of flower-like ZnO nanorods by thermal evaporation method, *Appl. Surf. Sci.*, 2011, **257**(11), 5083–5087.
- 38 A. Mathialagan, M. Manavalan, K. Venkatachalam, F. Mohammad, W. C. Oh and S. Sagadevan, Fabrication and physicochemical characterization of g-C<sub>3</sub>N<sub>4</sub>/ZnO composite with enhanced photocatalytic activity under visible light, *Opt. Mater.*, 2020, **100**, 109643.
- 39 R. K. Murry, P. K. Gerner, P. A. Mays and V. W. Rodwell, *Harper's Textbook of Biochemistry*, Appleton & Lange, Stanford, 2000.
- 40 A. L. Holder, R. Goth-Goldstein, D. Lucas and C. P. Koshland, Particle-induced artifacts in the MTT and LDH viability assays, *Chem. Res. Toxicol.*, 2012, **25**(9), 1885–1892.

